Journal of Materials Chemistry

Cite this: J. Mater. Chem., 2012, 22, 17984

www.rsc.org/materials

PAPER

In-doped Ga_2O_3 nanobelt based photodetector with high sensitivity and wide-range photoresponse†

Wei Tian,*[ab] Chunyi Zhi,*[a] Tianyou Zhai,*[a] Shimou Chen,[a] Xi Wang,[a] Meiyong Liao,[c] Dmitri Golberg[a] and Yoshio Bando[ab]

Received 19th May 2012, Accepted 13th July 2012
DOI: 10.1039/c2jm33189f

Doping is an efficient way to tune the electrical and photoelectrical performances of one-dimensional semiconductors which have potential application as active materials in high performance nanoscale devices. Ga_2O_3 is one the most promising 1D semiconducting systems. However, controlled doping of Ga_2O_3 toward higher photoelectrical performances in Ga_2O_3-based photodetectors remains problematic. Herein high-quality In-doped Ga_2O_3 nanobelts are fabricated through a facile and effective thermal evaporation process. Their morphology and structure are systematically characterized. Indium has successfully been doped into the Ga_2O_3 nanobelts based on the data obtained. The In-doped Ga_2O_3 nanobelt-based photodetector has shown a higher sensitivity (9.99×10^4%), responsivity (5.47×10^2 A W^{-1}), quantum efficiency (2.72×10^5%) and less rise/decay time (1/0.6 s), *i.e.* much better figures compared with not only the undoped Ga_2O_3 nanobelt/film but also other reported doped photodetectors. In addition, the above photodetector has a wider range photoresponse. In doping has led to significant improvements in the values of key parameters of the Ga_2O_3-based photodetector, beneficial for the fabrication of high-performance photodetectors.

1. Introduction

One-dimensional (1D) nanostructures have become the focus of worldwide research due to their potential use as active materials in high performance nanoscale devices and their high surface-to-volume ratios, and rationally designed surfaces.[1–6] Monoclinic gallium oxide (β-Ga_2O_3) is a chemically and thermally stable compound with an optical band gap of 4.9 eV. It is a promising candidate for application in optoelectronic devices including flat-panel displays, solar energy conversion devices and optical limiters for ultraviolet and high temperature stable gas sensors.[7–12] Recently, a lot of effort has been made to synthesize β-Ga_2O_3 nanowires or nanobelts by several research groups.[13–15] For example, Ga_2O_3 nanowires were synthesized by a simple physical evaporation method in an oxygen atmosphere using GaN powder as a raw material and an Al_2O_3 substrate with an indium layer as a catalyst.[13] Long Ga_2O_3 nanowires were prepared through thermal evaporation of Ga/Ga_2O_3 powders in the presence of Au catalyst and their optical properties were studied.[14] Long straight Ga_2O_3 nanowires were fabricated by the vapor–liquid–solid method and their optical wave-guiding properties were analyzed.[15] All these works have been focused on the synthesis and understanding of the basic properties of β-Ga_2O_3 nanowires. But the intentional control of their electrical and photoelectrical properties is still a challenging issue on the way toward their real applications in future optoelectronic devices.

Doping is an efficient way to tune the electrical and photoelectrical performances of semiconductors. It has been widely utilized in the semiconductor industry.[16–20] For example, N-doped ZnS nanoribbons show stable and reproducible transport properties, whereas undoped ZnS nanostructures are insulating;[21] Al-doped ZnO nanowires possess highly sensitive photo responses under below-gap light illumination, but undoped ZnO nanowires are optically inert.[17] S doping in In_2Se_3 nanowires leads to significant improvements in the transport and photoelectronic performances, enhancing the conductivity and improving the sensitivity to visible light.[22] Considerable efforts have been made to synthesize and tune the properties of variously doped Ga_2O_3 nanostructures,[23–25] but still the most efficient and simple way has not been found; this needs additional work. Furthermore, controlled doping of these nanostructures resulting in a corresponding photoelectrical performance improvement has never been reported.

[a]*International Center for Materials Nanoarchitectonics (WPI-MANA), National Institute for Materials Science (NIMS), 1-1 Namiki, Tsukuba, Ibaraki, 305-0044, Japan. E-mail: WEI.Tian@nims.go.jp; ZHI.Chunyi@nims.go.jp; ZHAI.Tianyou@nims.go.jp*
[b]*Department of Nano-Science and Nano-Engineering, Faculty of Science and Engineering, Waseda University, 3-4-1 Okubo, Shinjuku, Tokyo 169-8555, Japan*
[c]*Sensor Materials Center, NIMS, 1-1 Namiki, Tsukuba, Ibaraki, 305-0044, Japan*
† Electronic supplementary information (ESI) available. See DOI: 10.1039/c2jm33189f

Herein, we demonstrate a simple Au-assisted thermal evaporation approach to controllably synthesize high-quality, uniform In-doped Ga_2O_3 nanobelts. Then, detailed electrical and photoelectrical characteristics of individual In-doped Ga_2O_3 nanobelt based photodetectors were investigated. It was found that In doping had led to the significant improvements in the photoelectronic properties of Ga_2O_3 nanostructures, as required for the fabrication of high-performance Ga_2O_3-based photodetectors.

2. Experimental section

Synthesis of In-doped Ga_2O_3 nanobelts and undoped Ga_2O_3 nanobelts was carried out in a horizontal tube furnace through a CVD process as follows. For In-doped Ga_2O_3 nanobelts, a Ga_2O_3 powder, an In powder and a graphite powder were mixed in the molar ratio of 5 : 1 : 2 and used as the source material. Cleaned Au-coated Si (100) substrates were placed upward in an alumina boat to collect the products. The temperature in the center of the furnace was increased to 1000 °C in 30 min and maintained for 60 min. An Ar flow at a total flow rate of 200 sccm (standard cubic centimeter per minute) was used as the carrier gas. The furnace power was then switched off and the material was allowed to cool naturally to room temperature after the growth. For the undoped Ga_2O_3 nanobelts, the synthesis process was similar except that no In powder was used. The as-prepared samples were characterized using powder X-ray diffraction (XRD, RINT 2200HF), field-emission SEM (Hitachi-4800), and TEM (JEM-3000F) equipped with an X-ray energy dispersive spectrometer (EDS).

To fabricate single-nanobelt detectors, the nanostructures were removed by sonication from the substrate and subsequently dispersed in ethanol. The solution was dropped on a thermally oxidized Si substrate covered with a 200 nm SiO_2 layer. Two electrodes, together with their bonding pads, were exposed by electron-beam lithography. After development, a Cr/Au (10 nm/100 nm) film was deposited over the structure followed by a lift-off process. The current–voltage (I–V) characteristics of the devices were measured in air and room temperature using an Advantest picoampermeter R8340A and a dc voltage source R6144 under light illumination or in dark conditions. A spectral response for different wavelengths was recorded using a 500 W Ushio xenon lamp with an illumination bandwidth of 2 nm, and an Acton Research monochromator with order sorting filters was used. A time-dependent photocurrent response under 250 nm light illumination for the light-on and light-off states at a fixed applied voltage was detected, and the incident light power was calibrated by UV-enhanced Si photodiodes. For electrical measurements, gate voltages were applied to a n^+-Si substrate in a standard global back-gate geometry.

3. Results and discussion

The morphologies and crystal structures of the as-prepared undoped and doped Ga_2O_3 nanobelts are shown in Fig. 1. Typical scanning electron microscopy (SEM) images of the product in Fig. 1a–d show abundant undoped and In-doped Ga_2O_3 nanobelts, respectively, with a length of up to hundreds micrometers. The belts' widths and thicknesses are 200 nm to 1 μm, and 50–200 nm, respectively. The nanobelts' surfaces are smooth and clean without visible contaminations. It should be noted that the morphology of doped Ga_2O_3 does not show visible differences compared with that of the undoped compound. Comparative X-ray diffraction (XRD) patterns of the as-synthesized undoped and doped Ga_2O_3 nanobelts are shown in Fig. 1e. Except for the Si (100) peak from the substrates, all the diffraction peaks exclusively correspond to β-Ga_2O_3 (JCPDS 41-1103). Notably, the diffraction peaks from the doped sample are slightly shifted to lower angles relative to the undoped one, indicating a lattice parameter increase along the c-axis. This lattice expansion should be attributed to the incorporation of In into the Ga_2O_3 lattice: In^{3+} (0.8 Å) has a larger ionic radius than Ga^{3+} (0.62 Å).[26] The atomic models of undoped and doped nanobelts are shown in Fig. S1 and S2.†

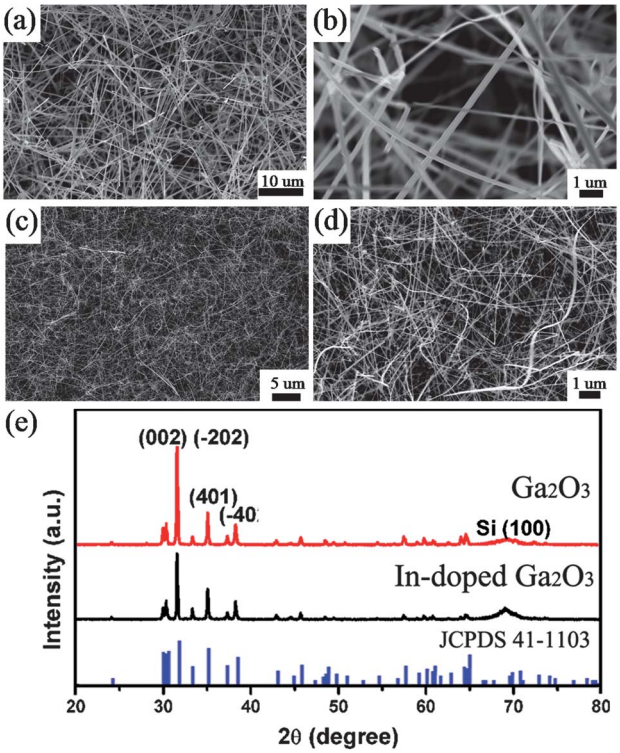

Fig. 1 (a and b) SEM images of abundant Ga_2O_3 nanobelts. (c and d) SEM images of In-doped Ga_2O_3 nanobelts. (e) Comparative XRD patterns of the Ga_2O_3 nanobelts and In-doped Ga_2O_3 nanobelts.

The typical transmission electron microscopy (TEM) image in Fig. 2a also displays a well-defined belt geometry with smooth sidewalls and a uniform diameter along the entire structure length. The high resolution transmission electron microscopy (HRTEM) image in Fig. 2b unveils clear lattice fringes, thereby indicating that the Ga_2O_3 nanobelts are structurally uniform and contain no defects, such as dislocations or stacking faults, suggesting the crystal quality of the Ga_2O_3 nanobelts has not been considerably affected by In incorporation. The marked spacings of ≈0.23 nm for the lattice fringes agree well with the expected separations of the $(\bar{3}11)$ planes in Ga_2O_3. Energy-dispersive X-ray spectroscopy (EDS) analysis was further performed to evaluate the In concentration in the doped Ga_2O_3 nanobelts. Besides the strong Ga and O signals (the Cu signals come from

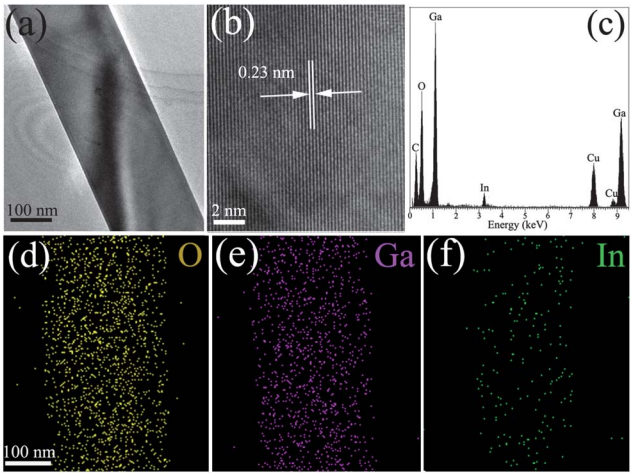

Fig. 2 (a) A typical TEM image of an individual In-doped Ga_2O_3 nanobelt. (b) HRTEM image of an individual In-Ga_2O_3 nanobelt. (c) The corresponding EDS pattern. (d–f) O, Ga, and In spatially resolved elemental maps, respectively.

the TEM grid), a small peak corresponding to In is apparent. Quantitative analysis reveals that the In concentration was about 0.8 at.%. Compositional spatial distribution was determined by the EDS elemental mapping, as shown in Fig. 2d–f, which reveals that In is uniformly distributed within the Ga_2O_3 nanobelt. The above results demonstrate that In was perfectly incorporated into the Ga_2O_3 nanobelts by the designed method.

Then, field-effect transistors (FETs) based on individual undoped and In-doped Ga_2O_3 nanobelts were fabricated, and their electrical properties were studied. Fig. 3a and b present the gate-dependent drain-source current (I_{DS}) *versus* voltage (V_{DS}) curves recorded on a representative single FET device. The doped device exhibits notable gate dependence and is conductive, reaching a current of 23 nA at a V_{DS} of −10 V and a gate voltage (V_G) of 40 V. The nonlinear curves indicate that Schottky barriers form between the Cr/Au electrodes and the nanobelt. Under a positively increasing V_G (0 → 40 V), the conductance of the nanobelt also increases, revealing an n-type conductivity. It has been reported that the pure Ga_2O_3 nanowires are normally n-type semiconductors due to oxygen vacancies.[27] The present nanobelts exhibit similar n-type semiconducting behavior. The undoped Ga_2O_3 nanobelts show similar behavior, but possess much lower currents. The undoped Ga_2O_3 nanowire has a lower conductivity (around 10^{-7} S cm^{-1}), while the doped one exhibits an enhanced conductivity (around 5.1×10^{-5} S cm^{-1}). It is known that the conductivity of undoped Ga_2O_3 mainly originates from O vacancies that are native donors, and therefore, the lower conductivity of the undoped nanobelts is likely due to a higher crystal quality and fewer defects, consistent with the structure characterization presented above.

We further estimate the carrier concentration and mobility in the doped nanobelts. The conventional method to obtain such parameters is to analyze their field-effect behavior using an FET setup. However, herein the Schottky barriers play an important role in the electron transport and the FET model may result in an underestimate of the mobility.[28] In fact, the present device, as a metal–semiconductor–metal (MSM) structure, can be modeled

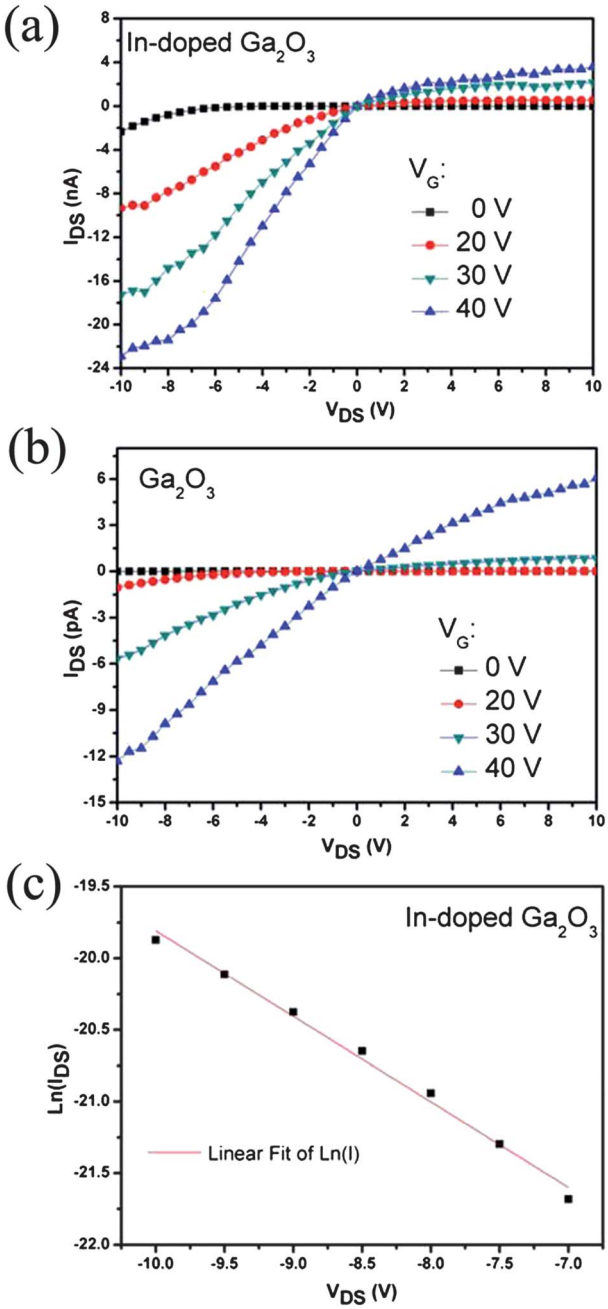

Fig. 3 (a) I_{DS}–V_{DS} plots at different V_G at 300 K for an In-doped Ga_2O_3 nanobelt device. (b) I_{DS}–V_{DS} plots at different V_G for an undoped Ga_2O_3 nanobelt device. (c) Experimental and fitted ln(I_{DS})–V plots at an intermediate bias at $V_G = 0$.

by two back-to-back Schottky barriers in series with a resistor in between. Considering that the tunneling current becomes dominant under a reverse bias in a low-dimensional system, thermionic field emission theory is proposed for analyzing the present semiconductor parameters from the two-terminal I–V curves.[29,30] In detail, the reverse-biased Schottky barrier dominates the total current in the intermediate bias regime of the I_{DS}–V_{DS} curve ($V_G = 0$):

$$\ln I = \ln(JS) = \ln S + V[(q/kT) - (1/E_0)] + \ln J_S$$

where J is the current density through the Schottky barrier, S is contact area, J_S is a slowly varying function of the applied bias, and $E_0 = E_{00}\coth(qE_{00}/kT)$ with $E_{00} = h/2[n/(m_{n^*}\varepsilon_s\varepsilon_0)]^{1/2}$, n is electron concentration, m_{n^*} and ε_s are the effective mass of an electron and relative permittivity of the material, respectively, and ε_0 is permittivity of free space. The logarithmic plot of a current I as a function of bias V gives approximately a straight line with a slope $q/(kT) - 1/E_0$, as depicted in Fig. 3c. Then n can be obtained *via* E_0, and the electron mobility can be calculated using $\mu = \sigma/(nq)$, with σ being the conductivity of the nanobelt. Applying this procedure to the I–V curves and assuming the relevant physical constants, such as m_{n^*} and ε_s (for Ga_2O_3, $m_{n^*} \approx 0.342m_e$, $\varepsilon_s \approx 10$, m_e being the free electron mass),[31–33] the electron concentration of the In-doped nanowire is estimated to be 9.66×10^{16} cm^{-3}, and the electron mobility is calculated to be 3.3×10^{-3} cm^2 V^{-1} S^{-1}. Therefore, on the basis of the above-discussed comparison, it is believed that the electrical behavior of the present doped nanobelt is greatly modulated by In doping.

Ga_2O_3 possesses a direct wide bandgap and has potential applications in optoelectronic devices, such as photodetectors and solar cells. To assess the photoelectrical properties of the doped Ga_2O_3 nanobelts, photodetectors based on individual doped and undoped nanostructures were constructed. The set-up of a photoconductive device for the photoresponse measurements on an individual nanobelt is shown in Fig. 4a. A monochromatic light illuminated the nanobelt connected to one pair of Cr/Au electrodes, and the photoresponse was measured by using a two-probe method. To decently compare the undoped and doped nanobelts detectors, we choose devices of a similar width and channel length from among numerous devices prepared. The insets of Fig. 4b and c show the SEM images of typical devices, in which the nanobelt width and channel length are approximately 460 nm and 1.9 μm, respectively. Fig. 4b and c represent the comparative spectral response of the undoped and doped Ga_2O_3 nanobelt photodetectors at a 6.0 V bias at room temperature. The undoped photodetector shows a high sensitivity to deep ultraviolet light with a cutoff wavelength of 260 nm. This corresponds to a photon energy that is close to the bandgap (4.9 eV, 260 nm) of Ga_2O_3 and implies a bandgap excitation related process. With further decreasing the wavelength (increasing the phonon energy), the responsivity gradually increases and reaches a maximum value at 250 nm. It is worth noting that the responsivity at 250 nm is about 3 orders of magnitude higher than that in the ultraviolet and visible light ranges, which indicates that the present photodetector is intrinsically "solar-blind". For the doped one, the preferred optical range is generally similar, showing a high sensitivity to deep ultraviolet light. However, the latter has a responsivity within a larger range, from 210–310 nm, revealing the smaller band gap arising from In doping.

Fig. 5a and b show the comparative I–V curves of In-doped Ga_2O_3 nanobelt-based and undoped Ga_2O_3 nanobelt-based photodetectors exposed to 250 nm 19 μW cm^{-2} light and under dark conditions. The I–V curves display a nonlinear behavior, which may be attributed to the Schottky barriers at the metal–semiconductor contacts.[34] For the doped nanobelt, an enhancement of current is observed when the device is illuminated using a 250 nm light with the energy above the threshold excitation energy, E_g (<4.9 eV, 260 nm). At a fixed voltage of 6.0 V, the photocurrent (91 pA) is about 910 times larger than the dark current (0.1 pA). Such an increase in current is attributed to the electron–hole pairs being excited by the incident light, which has an energy larger than the band gap, and also to the desorption of oxygen at the nanobelt surface.[35,36] For the undoped case, a similar phenomenon is seen when the device is illuminated, except a smaller photocurrent. At a voltage of 6 V, the photocurrent is ~5.3 pA, much smaller than in the doped case. These results indicate that the photocurrent dramatically increases after In-doping. A corresponding logarithmic plot (Fig. 5c) clearly

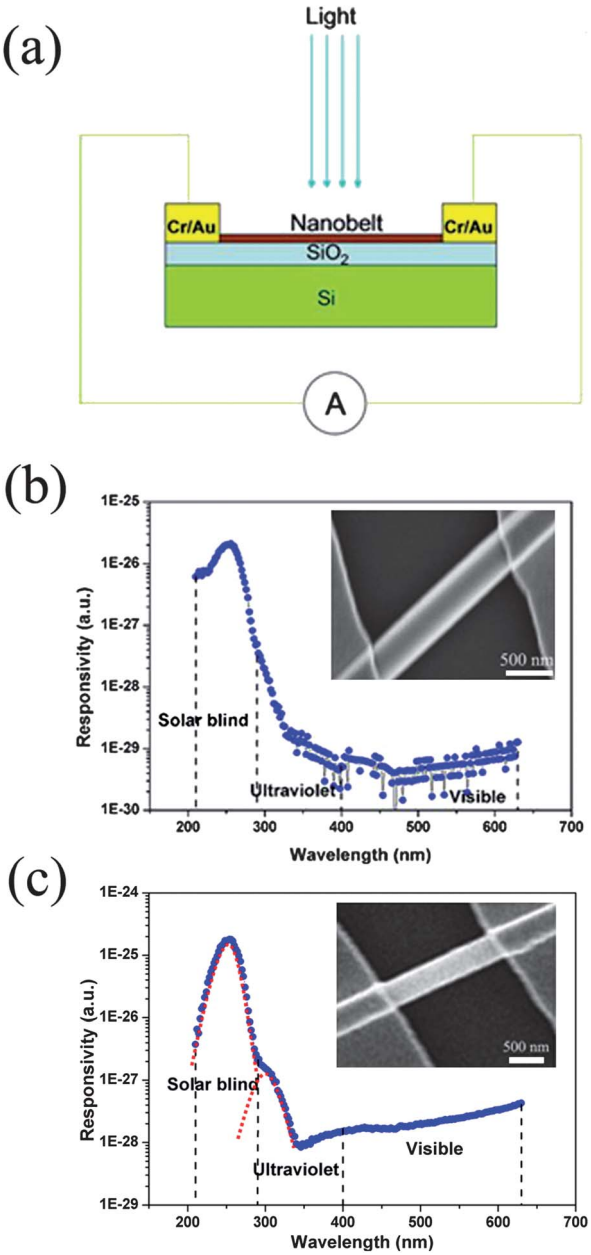

Fig. 4 (a) Schematic of an individual nanobelt photodetector. (b) Spectral response of an individual Ga_2O_3 nanobelt photodetector. The inset is a typical SEM image of a Ga_2O_3 nanobelt device. (c) Spectral response of an individual In-doped Ga_2O_3 nanobelt photodetector. The inset is a typical SEM image of an individual In-doped Ga_2O_3 nanobelt device.

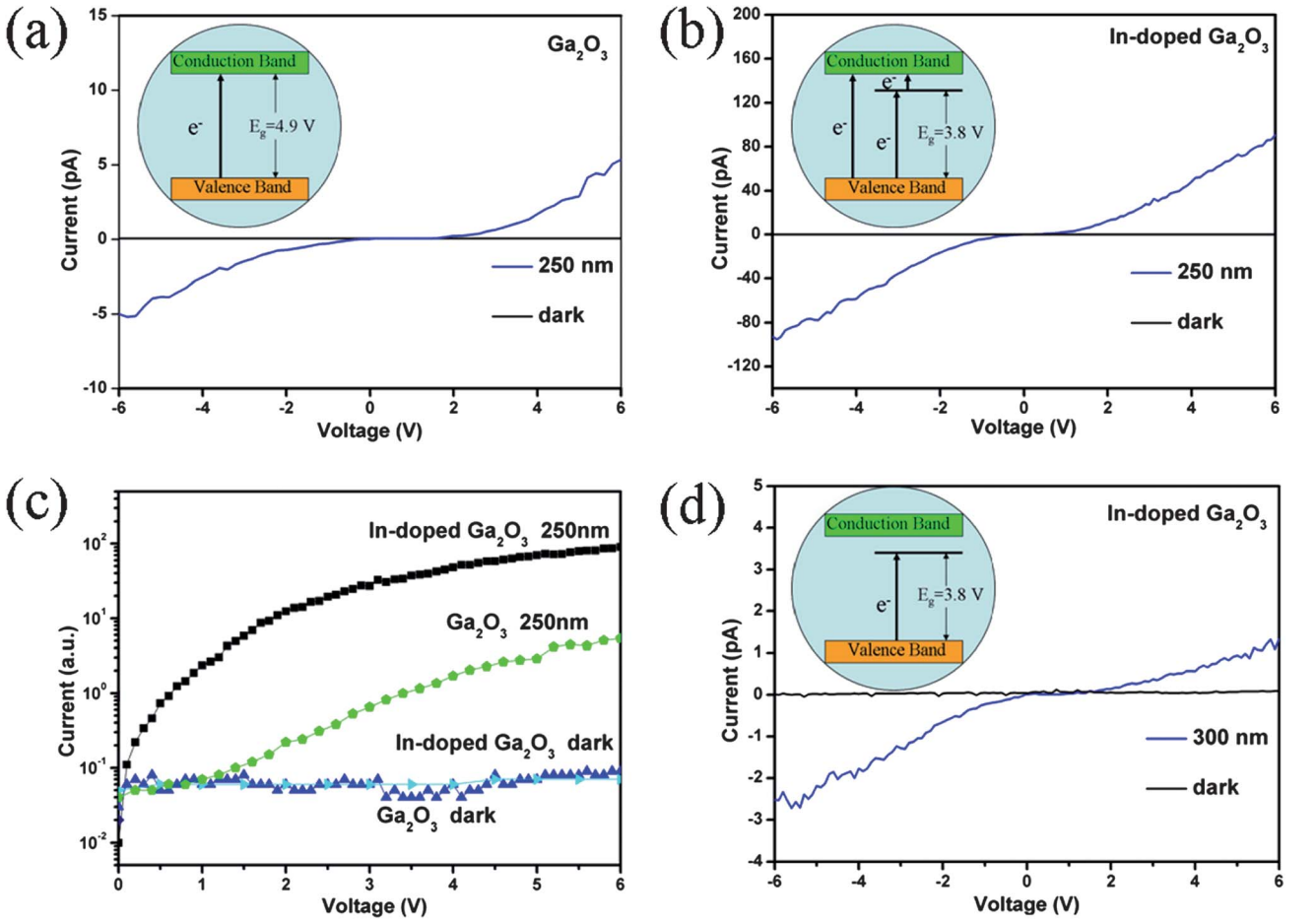

Fig. 5 (a) *I–V* curves of the individual Ga_2O_3 nanobelt photodetector. The inset is the schematic band diagram of Ga_2O_3. (b) In-doped Ga_2O_3 nanobelt photodetector under illumination with the 250 nm wavelength light and in dark conditions. The inset is the schematic band diagram of In-doped Ga_2O_3. (c) Logarithmic plot of (a) and (b). (d) In-doped Ga_2O_3 nanobelt photodetector under 300 nm light. The inset is the schematic band diagram of In-doped Ga_2O_3 under 300 nm light illumination.

shows that the ratio of photo current to dark current of the undoped nanobelt photodetector is around 10^2. As for the doped one, this value increases to 10^3, indicating much higher sensitivity. Fig. 5d shows the *I–V* curves of the doped nanobelt device illuminated by a 300 nm light (*i.e.* with a lower energy than the band gap of Ga_2O_3). It is worth noting that the device still exhibits a photocurrent of ~2 pA at 6 V, demonstrating a smaller band gap after In doping. This can be explained by the fact that In doping[16–22] results in a mid-band gap energy level which reduces the energy gap required for charge separation, as shown in the schematic band diagram in the insets of Fig. 5a, b and d. Therefore, the doped nanobelt displays a higher photocurrent than the undoped device under 250 nm light illumination. In addition, the In-doped photodetector has a wide-range photoresponse.

The time response is usually the key factor for sensor performance and it determines the capability of a photodetector to follow a fast-varying optical signal. Fig. 6a and b show the comparative time responses of the undoped and doped nanobelt devices, respectively, under pulsed incident 250 nm light created by a manual chopper. During illumination ON, the current of the undoped nanobelt photodetector rapidly increases to a stable value of ~8 pA, and then sharply returns to its initial value as the light is turned OFF, indicating the excellent stability and reproducible characteristics of the device. For the doped case, the same phenomena are seen except for a much larger photo current in the latter case. It should be noted that the detection limit of our current (dc) picoampermeter is 0.3 s. The time intervals taken for the current to increase from 10% to 90% of the peak value or *vice versa* are defined as T_r and T_d, respectively. Under closer examination, T_r and T_d of the undoped detector are ≈2.4 s and <0.6 s, respectively. For the doped one, these values become ≈1 s and <0.6 s, respectively. Therefore, the response time shows a small decrease. The regarded values are comparable with those of many reported and prospective 1D nanostructure-based photodetectors. It is worth noting that the response time is longer than the decay time for both present devices studied. Since the increase of a photocurrent is related to the process of desorption of oxygen at the nanobelt surface, which is a relatively slow process, the response time is becoming a little longer. However, when the light is OFF, the current decreases quickly due to the larger resistivity of the device.

The sensitivity of the photodetector, defined as $(I_{photo} - I_{dark})/I_{dark}$ in percent, the spectra responsivity (R_λ), defined as the

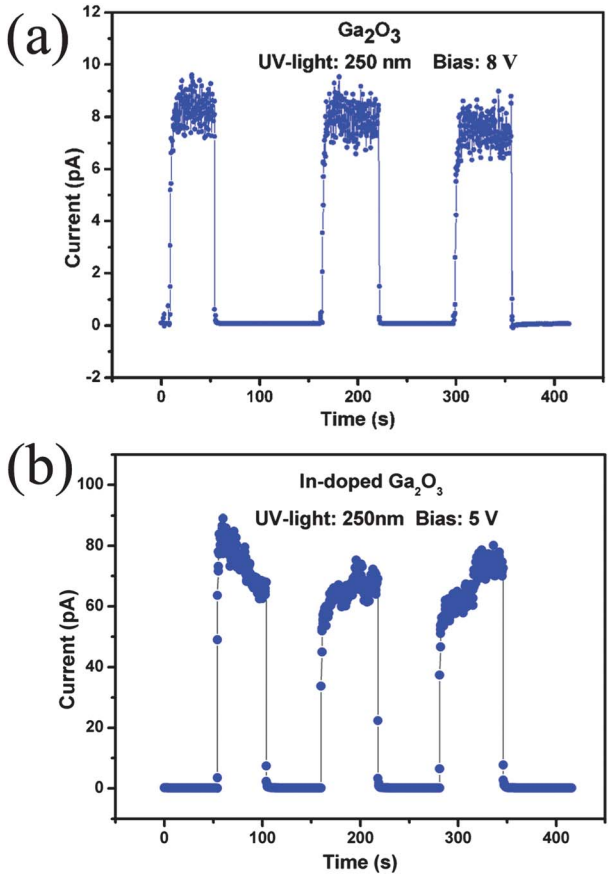

Fig. 6 (a) Time response of an individual Ga_2O_3 nanobelt at a bias voltage of 8 V. (b) Time response of an individual In-doped Ga_2O_3 nanobelt at a bias voltage of 5 V.

photocurrent generated per unit power of incident light on the effective area of a photoconductor, and the external quantum efficiency (EQE), defined as the number of electrons detected per incident photon, are the key parameters to evaluate the performance of a photodetector. The larger values of sensitivity, R_λ and EQE – the higher performance a photodetector has. The R_λ and EQE can be calculated using equations: $R_\lambda = I/PS$ and EQE = $hcR_\lambda/e\lambda$, where I is the difference between a photocurrent and a dark current, P is light intensity, S is effective illuminated area, h is Planck's constant, c is velocity of light, e is electronic charge and λ is excitation wavelength. Remarkably, the calculated sensitivity, R_λ and EQE for the In-doped Ga_2O_3 nanobelts are as high as 9.09×10^4%, 5.47×10^2 A W^{-1} and 2.72×10^5%, respectively, for the incident wavelength of 250 nm at 6 V, which are not only higher than the values for the undoped Ga_2O_3 but also for most of the reported doped photodetectors,[17,22,28,37–44] as summarized in Tables 1 and 2.

The large photo-dark current ratio, high sensitivity, fast response and high R_λ (or EQE) may be ascribed to the chemically pure, high-quality single crystals grown, their large surface-to-volume ratio, shorter channel length, and lower recombination barrier.[45–48] Several unique characteristics of the present In-doped Ga_2O_3 nanobelt devices are thought to significantly improve the observed responsivity compared to the previous devices: (1) superior crystal quality (the density of traps induced by defects is thus dramatically reduced and the photocurrent rapidly reaches a steady state both on rise and decay stages). (2) Larger surface-to-volume ratio (the dangling bonds on the nanostructure surface can serve as recombination centers for photogenerated carriers, which would enhance the free carriers' recombination and shorten the decay time). (3) Shorter channel (a short channel can result in shortening the photocarrier transit time, thus increasing the responsivity). (4) Lower recombination barrier (band bending usually occurs at the semiconductor surface due to Fermi-level pinning, which results in a recombination barrier for electron–hole pairs).

Furthermore, according to Garrido's photoconductive gain model for GaN photodetectors,[49] the current increment of the present nanobelt device caused by conductive volume modulation can be written as:

$$\Delta I = W(W_{\text{dark}} - W_{\text{illum}})q\mu n V_{\text{bias}}/L$$

where ΔI is the measured current difference between dark and photo currents, W_{dark} is the surface depletion region (SDR) width in the dark, W_{illum} is the SDR width under light, W is the nanobelt width, L is the device channel length, q is electron charge, μ is electron mobility, n is carrier density and V_{bias} is applied bias voltage. Since the values of W, L, W_{dark}, W_{illum} and V_{bias} are similar for both undoped and doped photodetectors, ΔI is mainly determined by μ and n. Obviously, μ and n values for the doped nanobelt are larger than those for the undoped one, which is also confirmed by the documented electrical performance. What's more, according to Prades' systematic studies of a photodetector based on individual n-type nanowire, the photocurrent I_{photo} is given by the equation:[50]

$$I_{\text{photo}} = q(W/L)\beta\eta\tau\mu V_{\text{bias}}\Phi_{\text{ph}}$$

where three different contributions are clearly identified. The first one is related to geometric parameters of the device (W/L), the second one to the intrinsic properties of nanobelts ($\beta\eta\tau\mu$), and

Table 1 Comparison of the characteristic parameters for undoped Ga_2O_3 semiconductor photodetectors from previous reports with the present work

Photodetector	Spectral responsivity/A W^{-1}	EQE/%	Photo-dark current ratio	Ref.
Ga_2O_3 nanowire	33.7	1.67×10^4	4.0×10^2	28
Ga_2O_3 nanowire	—	—	3.7–21.5	37
Ga_2O_3 thin film	8×10^{-5}	—	—	38
Ga_2O_3 single crystal	2.6–8.7	—	$\approx 10^2$	39
Ga_2O_3 nanobelt	—	—	6.67×10^2	40
Ga_2O_3 nanobelt	32	1.59×10^4	10^2	This work
In-doped Ga_2O_3 nanobelt	5.47×10^2	2.72×10^5	9.10×10^2	This work

Table 2 Comparison of the characteristic parameters for doped 1D inorganic semiconductor photodetectors from previous reports with the present work

Photodetector	Spectral responsivity/A W^{-1}	EQE/%	Photo-dark current ratio	Sensitivity/%	Rise time/s	Decay time/s	Ref.
Al-doped ZnO nanowire	—	—	≈20	1.9×10^3	—	—	17
S-doped In_2Se_3 nanowire	1.3×10^3	3.3×10^5	9.4	9.3×10^2	—	—	22
Co-doped ZnO nanobelt	—	—	84.6	8.36×10^3	≈60	250	41
Cu-doped ZnO nanobelt	4.0×10^2	1.7×10^5	$\approx 10^2$	9.9×10^3	9	17	42
Sb-doped ZnO nanobelt	—	—	23	2.2×10^3	—	—	43
In-doped CdSe nanowire	—	—	2.2	2.1×10^2	<30	>60	44
In-doped Ga_2O_3 nanobelt	5.47×10^2	2.72×10^5	9.10×10^2	9.09×10^4	≈1	<0.6	This work

the third one only depends on the experimental conditions ($V_{bias}\Phi_{ph}$). Considering that the values of β (the fraction of photons not reflected by the surface), η (the quantum efficiency of carrier generation by one photon), and τ (carrier lifetime) are similar for the undoped and doped nanobelts, the larger μ (carrier mobility) contributes to the larger photocurrent. It has been known that doping is an efficient way to increase the sensitivity and responsivity of a photodetector. In fact, it has clearly been demonstrated in our work based on the above-discussed models.

4. Conclusions

In summary, we developed a facile and effective thermal evaporation process for the synthesis of high-quality In-doped Ga_2O_3 nanobelts. Their morphology and structure were systematically investigated. Successful doping was verified by XRD and EDS-mapping results. The detailed electrical and photoelectrical characteristics of individual undoped and In-doped Ga_2O_3 nanobelt based photodetectors were investigated. The In-doped Ga_2O_3 nanobelt based devices showed a higher sensitivity (9.09×10^4%), responsivity (5.47×10^2 A W^{-1}), quantum efficiency (2.72×10^5%) and shorter rise/decay time (1/0.6 s); the parameters which are superior compared with not only the undoped Ga_2O_3 devices but also reported doped photodetectors. Indium doping led to significant improvements in photoelectronic properties of Ga_2O_3 nanostructures. These are beneficial for the fabrication of high-performance future Ga_2O_3-based optoelectronic nanodevices and their smart integration into technology.

Acknowledgements

This work was supported by the World Premier International Center for Materials Nanoarchiterctonics (WPI-MANA), National Institute for Materials Science, Japan.

Notes and references

1 Y. N. Xia, P. D. Yang, Y. G. Sun, Y. Y. Wu, B. Mayers, B. Gates, Y. D. Yin, F. Kim and H. Q. Yan, *Adv. Mater.*, 2003, **15**, 353.
2 C. W. Cheng, B. Liu, H. Y. Yang, W. W. Zhou, L. Sun, R. Chen, S. F. Yu, J. X. Zhang, H. Gong, H. D. Sun and H. J. Song, *ACS Nano*, 2009, **3**, 3069.
3 G. Z. Shen, D. Chen, P. C. Chen and C. W. Zhou, *ACS Nano*, 2009, **3**, 1115.
4 X. S. Fang, Y. Bando, U. K. Gautam, T. Y. Zhai, H. B. Zeng, X. J. Xu, M. Y. Liao and D. Golberg, *Crit. Rev. Solid State Mater. Sci.*, 2009, **34**, 190.
5 T. Y. Zhai, X. S. Fang, Y. Bando, B. Dierre, B. D. Liu, H. B. Zeng, X. J. Xu, Y. Huang, X. L. Yuan, T. Sekiguchi and D. Golberg, *Adv. Funct. Mater.*, 2009, **19**, 2423.
6 C. H. Ye, Y. Bando, G. Z. Shen and D. Golberg, *Angew. Chem., Int. Ed.*, 2006, **45**, 4922.
7 D. Edwards, T. O. Mason, F. Goutenoir and K. R. Peoppel, *Appl. Phys. Lett.*, 1997, **70**, 1707.
8 M. O. Gita, N. Saika, Y. Nakanishi and Y. Hatanaka, *Appl. Surf. Sci.*, 1999, **142**, 188.
9 Z. J. Hajnal, J. Miró, G. Kiss, F. Réti, P. Deák, R. C. Herndon and M. J. Kuperberg, *Appl. Phys. Lett.*, 1999, **86**, 3792.
10 L. Binet and D. J. Gourier, *J. Phys. Chem. Solids*, 1998, **59**, 1241.
11 M. Ogita, K. Higo, Y. Nakanishi and Y. Hatanaka, *Appl. Surf. Sci.*, 2001, **175**, 721.
12 M. Fleischer, S. Kornely, T. Weh, J. Frank and H. Meixner, *Sens. Actuators, B*, 2000, **69**, 205.
13 J. Zhang and F. H. Jiang, *Chem. Phys.*, 2003, **289**, 243.
14 X. Xiang, C. B. Cao and H. S. Zhu, *J. Cryst. Growth*, 2005, **279**, 122.
15 F. Wang, Z. H. Han and L. M. Tong, *Phys. E.*, 2005, **30**, 150.
16 Z. B. He, J. S. Jie, W. J. Zhang, W. F. Zhang, L. B. Luo, X. Fan, G. D. Yuan, I. Bello and S. T. Lee, *Small*, 2009, **5**, 345.
17 D. D. Lin, H. Wu and W. Pan, *Adv. Mater.*, 2007, **19**, 3968.
18 U. K. Gautam, L. S. Panchakarla, B. Dierre, X. S. Fang, Y. Bando, T. Sekiguchi, A. Govindaraj, D. Golberg and C. N. R. Rao, *Adv. Funct. Mater.*, 2009, **19**, 131.
19 S. L. Ji, L. L. Yin, G. D. Liu, L. D. Zhang and C. H. Ye, *Chem. Commun.*, 2009, 2344.
20 S. L. Ji, L. L. Yin, G. D. Liu, L. D. Zhang and C. H. Ye, *J.Phys. Chem. C*, 2009, **113**, 16439.
21 G. D. Yuan, W. J. Zhang, W. F. Zhang, X. Fan, I. Bello, C. S. Lee and S. T. Lee, *Appl. Phys. Lett.*, 2008, **93**, 213102.
22 T. Y. Zhai, Y. Ma, L. Li, X. S. Fang, M. Y. Liao, Y. Koide, J. N. Yao, Y. Bando and D. Golberg, *J. Mater. Chem.*, 2010, **20**, 6630.
23 S. Ohira, N. Suzuki, N. Arai, M. Tanaka, T. Sugawara, K. Nakajima and T. Shishido, *Thin Solid Films*, 2008, **516**, 5763.
24 G. C. Liu, X. C. H. Duana, H. B. Li and D. W. Liang, *Mater. Chem. Phys.*, 2008, **110**, 206.
25 G. Q. Pei, C. T. Xia, Y. J. Dong, B. Wu, T. Wang and J. Xu, *Scr. Mater.*, 2008, **58**, 943.
26 Y. B. Tang, X. H. Bo, J. Xu, Y. L. Cao, Z. H. Chen, H. S. Song, C. P. Liu, T. F. Humh, W. J. Zhang, H. M. Cheng, I. Bello, S. T. Lee and C. S. Lee, *ACS Nano*, 2011, **5**, 3591.
27 Y. Huang, Z. Wang, Q. Wang, C. Gu, C. Tang, Y. Bando and D. Golberg, *J. Phys. Chem. C*, 2009, **113**, 1980.
28 L. Li, E. Auer, M. Y. Liao, X. S. Fang, T. Y. Zhai, U. K. Gautam, A. Lugstein, Y. Koide, Y. Bando and D. Golberg, *Nanoscale*, 2011, **3**, 1120.
29 Z. Zhang, K. Yao, Y. Liu, C. Jin, X. Liang, Q. Chen and L. M. Peng, *Adv. Funct. Mater.*, 2007, **17**, 2478.
30 Z. Y. Zhang, C. H. Jin, X. L. Liang, Q. Chen and L. M. Peng, *Appl. Phys. Lett.*, 2006, **88**, 073102.
31 H. He, R. Orlando, M. A. Blanco and R. Pandey, *Phys. Rev. B: Condens. Matter Mater. Phys.*, 2006, **74**, 195123.
32 T. Oshima, T. Okuno, N. Arai, N. Suzuki, H. Hino and S. Fujita, *Jpn. J. Appl. Phys.*, 2009, **48**, 011605.
33 F. Zeng, X. Zhang, J. Wang, L. Wang and L. Zhang, *Nanotechnology*, 2004, **15**, 596.

34 J. Zhou, Y. D. Gu, Y. F. Hu, W. J. Mai, P. H. Yeh, G. Bao, A. K. Sood, D. L. Polla and Z. L. Wang, *Appl. Phys. Lett.*, 2009, **94**, 191103.
35 C. H. Lin, T. T. Chen and Y. F. Chen, *Opt. Express*, 2008, **16**, 16916.
36 Y. Muraoka, N. Takubo and Z. Hiroi, *J. Appl. Phys.*, 2009, **105**, 103702.
37 P. Feng, X. Y. Xue, Y. G. Liu, Q. Wan and T. H. Wang, *Appl. Phys. Lett.*, 2006, **89**, 112114.
38 Y. Kokubun, K. Miura, F. Endo and S. Nakagomi, *Appl. Phys. Lett.*, 2007, **90**, 031912.
39 T. Oshima, T. Okuno, N. Arai, N. Suzuki, S. Ohira and S. Fujjta, *Appl. Phys. Express*, 2008, **1**, 011202.
40 P. Feng, J. Y. Zhang, Q. H. Li and T. H. Wang, *Appl. Phys. Lett.*, 2006, **88**, 153107.
41 L. Peng, J. L. Zhai, D. J. Wang, P. Wang, Y. Zhang, S. Pang and T. F. Xie, *Chem. Phys. Lett.*, 2008, **456**, 231.
42 N. Kouklin, *Adv. Mater.*, 2008, **20**, 2190.
43 Y. Yang, W. Guo, J. J. Qi, J. Zhao and Y. Zhang, *Appl. Phys. Lett.*, 2010, **97**, 223113.
44 Z. B. He, J. S. Jie, W. J. Zhang, W. F. Zhang, L. B. Luo, X. Fan, G. D. Yuan, I. Bello and S. T. Lee, *Small*, 2009, **5**, 345.
45 T. Y. Zhai, X. S. Fang, M. Y. Liao, X. J. Xu, L. Li, B. D. Liu, Y. Koide, Y. Ma, J. N. Yao, Y. Bando and D. Golberg, *ACS Nano*, 2010, **4**, 1596.
46 R. Calarco, M. Marso, T. Richter, A. Aykanat, R. Meijers, A. V. D. Hart, T. Stoica and H. Luth, *Nano Lett.*, 2005, **5**, 981.
47 P. Kung, X. Zhang, D. Wallker, A. Saxler, J. Piotrowski, A. Rogalski and M. Razeghi, *Appl. Phys. Lett.*, 1995, **67**, 3792.
48 X. J. Zhang, J. S. Jie, W. F. Zhang, C. Y. Zhang, L. B. Luo, Z. B. He, X. H. Zhang, W. J. Zhang, C. S. Lee and S. T. Lee, *Adv. Mater.*, 2008, **20**, 2427.
49 J. A. Garrido, E. Monroy, I. Izpura and E. Munoz, *Semicond. Sci. Technol.*, 1998, **13**, 563.
50 J. D. Prades, R. J. Diza, F. H. Ramirez, L. F. Romero, T. Andreu, A. Cirera, A. R. Rodriguez, A. Conrnet, J. R. Morante, S. Barth and S. Mathur, *J. Phys. Chem. C*, 2008, **112**, 14639.